Journal of Materials Chemistry C

Accepted Manuscript

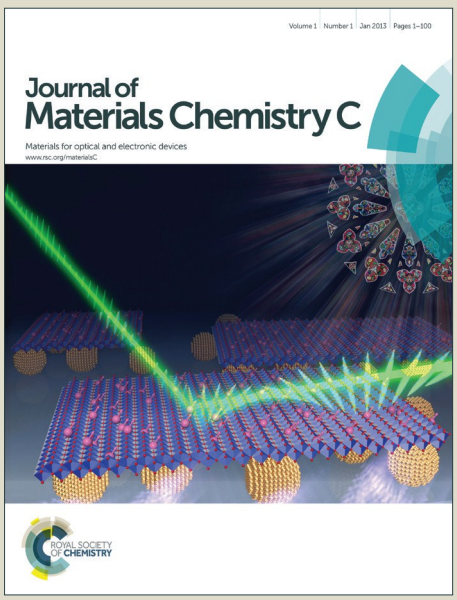

ROYAL SOCIETY OF CHEMISTRY

www.rsc.org/materialsC

Journal Name

ARTICLE TYPE

Cite this: DOI: 10.1039/xxxxxxxxxx

Unconventional properties of nanometric FeO(111) films on Ru(0001): stoichiometry and surface structure

Laura Martín-García,*[a] Iván Bernal-Villamil,*[b] Mohamed Oujja,[a] Esther Carrasco,[a] Raquel Gargallo-Caballero,[a] Marta Castillejo,[a] José F. Marco,[a] Silvia Gallego,[b] and Juan de la Figuera[a]

Received Date
Accepted Date

DOI: 10.1039/xxxxxxxxxx

www.rsc.org/journalname

We report on the growth of high quality monocrystalline and stoichiometric FeO(111) films on Ru(0001) by infrared pulsed laser deposition (IR-PLD), in a thickness range from below 1 nm to above 8 nm. The films are characterized by low-energy electron diffraction (LEED), X-ray photoelectron spectroscopy (XPS) and ion scattering spectroscopy (ISS). Besides the 1:1 Fe/O ratio, they show some unexpected properties, as the lack of Fe^{3+} sites at the surface, the (1×1) surface symmetry and the large lattice expansion. First-principles calculations evidence that these properties can be understood from the existence of a wurtzite-like environment at the surface region, that preserves the bulk-like antiferromagnetism. This extends the validity of stacking-faults as efficient mechanisms to compensate surface polarity, and suggests that surface-induced processes can be tailored to design nanoscaled materials beyond the parent bulk phase diagram.

At ambient conditions, bulk FeO is well known to present a large number of iron vacancies, in the range of 5-15%[1]. Ideally, bulk FeO has a cubic rock-salt lattice, where layers of Fe^{2+} cations and O^{2-} anions alternate along the [111] direction. Below a Néel temperature of 200K, it is antiferromagnetic, with adjacent ferromagnetic (111) cation planes holding opposite magnetization orientations. The antiferromagnetic order introduces a rhombohedral distortion along the [111] axis[2]. These structural, electronic and magnetic features are shared by the transition metal monoxides MnO, CoO and NiO, placing them as prototype materials in the study of band filling effects at complex phenomena that involve electronic correlations. Only the large concentration of cation vacancies is a singular property of FeO, particularly difficult to control due to their ease to rearrange even at low temperatures[3]. Furthermore, the Fe vacancies have a strong effect on the material properties, from lattice expansion to resistivity[4,5], and introduce local polaronic and magnetic features that resemble those of magnetite[6]. The resulting net magnetization is also a disadvantage in the current search for robust antiferromagnets to be exploited in low dimensional exchange bias systems, intended to reduce the critical thickness for the onset of superparamagnetism[7]. Good quality single crystal films of stoichiometric FeO could thus be of large interest, specially if the stoichiometry could be controlled independently.

FeO films of subnanometric thickness have received large attention in recent years due to their enhanced catalytic activity[8,9]. Films one and two monolayers thick can be grown even in thermodynamic conditions where other iron oxides, usually magnetite, should appear, for example, up to 2 atomic layers on Pt(111)[10], or up to 4 layers on Ru(0001)[11]. Even the growth of the stable iron oxide forms on different substrates takes place initially through FeO(111) layers (followed by Fe_3O_4/γ-Fe_2O_3)[12–15]. Though the detailed structural and magnetic properties of these films are not identical to those of the bulk form, they adopt the FeO stoichiometry and a rocksalt lattice structure. A common experimental feature for such films is the expansion of the in-plane lattice parameter with respect to the bulk value, typically 0.320 nm versus 0.304 nm[11,16]. This expansion has been related to a minimization of the Madelung energy to avoid the polar catastrophe in the ultrathin limit[11].

Previous efforts to synthetize thicker nanoscaled FeO films have resulted in samples with poor crystalline quality[17] or Fe^{3+} sites that evidence the presence of defects[18]. Typically, a (2×2) surface symmetry is obtained, indicative of structural or magnetic disorder, or of the onset of the evolution to magnetite[19–21]. At moderate thicknesses, measurements of magnetic order indicate the formation of FeO distinct from the known bulk form[22,23]. Usual growth methods for such nanoscaled films are either consecutive steps of iron metal deposition and film oxidation, or continuous

[a] Instituto de Química Física "Rocasolano", CSIC, Madrid E-28006, Spain.
[b] Instituto de Ciencia de Materiales de Madrid, CSIC, Madrid E-28049, Spain.
* These two authors contributed equally.

iron metal deposition under an oxygen background, i.e. reactive molecular beam epitaxy O-MBE[24]. The crucial influence of the preparation conditions adds challenging difficulties, as moderate variations of the oxygen pressure or the temperature during growth may result in different oxide phases. In this respect, the study by Spiridis et al[12] offers a tantalizing glimpse towards this goal: FeO films up to 4 nm could be grown by a careful optimization of the oxidation conditions, with a recovery of bulk-like features for thicknesses over 2 nm. However, thicker films revert to magnetite when using such growth method.

Besides O-MBE, another extensively used technique for growing films of a variety of materials with tailored properties is pulsed laser deposition (PLD)[25]. Nanostructured thin films with different properties in terms of size, shape, composition and crystallinity may be obtained by varying the laser and growth parameters. In this case, the growth conditions are out of equilibrium, with a large energy per atom deposited on the surface[26]. Although an ultraviolet wavelength is commonly employed for nanosecond PLD of oxides, we have successfully used an infrared wavelength of 1064 nm (i.e., IR-PLD) to grow highly crystalline magnetite films on several substrates[27,28].

In this work, we report the growth of unusually thick stoichiometric FeO(111) films on Ru(0001) by IR-PLD. The films are directly obtained by deposition from a hematite target onto a heated Ru(0001) substrate with no need of subsequent oxidation or post-annealing. We will further show that the films obtained with this procedure are single crystal and highly stoichiometric. Supported by first principles calculations, we will also demonstrate that the unusual surface properties of these films (lack of Fe^{3+} atoms under a (1×1) symmetry and expanded lattice parameter) can only be explained admitting a local wurtzite (WZ)-like surface environment, that to date has only been reported for O-ended CoO(111)[29]. The surface region extends few layers in depth, and bulk-like properties are then recovered even for the thinnest films. The layered antiferromagnetic order is preserved throughout the entire structure. Our results suggest that the existence of tetrahedral Fe^{2+} sites at the surface plays an active role in the stabilization of the undefected FeO nanostructures.

1 Methods

1.1 Experimental

The experiments were performed in a home-made multipurpose ultra-high vacuum (UHV) system consisting of a preparation chamber, where the PLD growth takes place, and a characterization chamber. Both chambers have a base pressure of 2×10^{-10} Torr. The preparation chamber accommodates several MBE sources together with a target holder with rotation control to avoid cratering, and a sample holder with a heating filament. The characterization chamber is equipped with a 4-grid low-energy electron diffractometer. A dual Mg/Al anode x-ray gun and an hemispherical Phoibos-150 analyzer are employed for in-situ x-ray photoelectron spectroscopy (XPS). The same analyser in combination with a differentially pumped ion gun are used for low ion scattering spectroscopy (ISS).

The substrate for IR-PLD was a Ru(0001) single crystal, previously used to grow FeO films by reactive-MBE[24]. To remove each FeO film and recovering a clean surface, the Ru substrate was subjected to cycles of 3.5 keV Ar^+ sputtering and heating flashes to 1573 K in UHV until the LEED pattern showed the Ru 1×1 pattern and no contaminants were detected by XPS.

Hematite (α-Fe_2O_3) pellets were used as targets. They were prepared by pressing hematite powder (Aldrich, >99% purity) into disks (10 mm diameter and 2 mm thickness) with an hydrostatic press (8 ton cm^{-2}) and sintered in air for 8 hours at 1173 K.

The hematite targets were ablated using a Q-switched Nd:YAG laser with a pulse duration of 5 ns and repetition rate of 10 Hz at the excitation wavelength of 1064 nm. The laser beam was focused onto the target at 45° to a spot area of 0.15 mm^2. The fluence (laser energy per unit area) used for fabrication of deposits was fixed to a value of 4.4 Jcm^{-2} corresponding to 8 times the ablation threshold fluence of the target. This threshold value was determined by measuring the minimum single pulse energy necessary to yield a luminous plume as detected by eye on the hematite target; and the diameter of the irradiated region by the print left on an unplasticized polyvinyl chloride sheet.

LEED patterns were recorded at an electron energy of 50 eV. The surface presented a uniform LEED pattern after preparation of each film. ISS spectra were acquired using He^+ ions with energies of 525 eV. The angle of incidence, defined as the angle of the ion beam with respect to the sample plane, was varied by rotation of the sample manipulator and the collecting angle was normal to the surface.

XPS data were acquired using Al Kα radiation ($h\nu$ = 1486.6 eV). All reported spectra were recorded at an electron take-off angle of 90° (unless explicitly mentioned) with a constant analyzer pass energy of 20 eV. All binding energies are referred to the Ru $3d_{5/2}$ signal, which was set to 280.0 eV. The spectra were fitted with pseudo Voight line profiles and a Shirley background using the CasaXPS software (version 2.3.16). The Lorentzian/Gaussian mixing ratio and FWHM were fixed along the series of spectra. The thickness of the pulsed laser deposited films was estimated by employing the relative areas of the Fe $2p$ and Ru $3d$ core level peaks and assuming that a uniform film was deposited. The film thickness was calculated according to[30]:

$$\frac{I_{ox}}{I_{sub}} = \frac{S_{ox}}{S_{sub}} \frac{[1-\exp(-z/\lambda_{ox})]}{\exp(-z/\lambda_{sub})}$$

where I_{ox} and I_{sub} stand for the areas of the Fe $2p$ and Ru $3d$ core level peaks, S_{ox} and S_{sub} refer to their respective atomic sensitivity factors and z is the thickness of the deposited film. These sensitivity factors (S) include the transmission function correction, the escape depth compensation and the relative sensitivity factors (CasaXPS RSF library) according to the evaluation spectra procedure of the selected software. The electron attenuation length at the kinetic energies of the Fe $2p$ core level peaks, λ_{ox}, and the corresponding one of the Ru $3d$ core level peaks, λ_{sub}, were obtained from the NIST electron effective-attenuation-length database[31]. Their numerical values are $\lambda_{ox} = 1.20$ nm and $\lambda_{sub} = 1.78$ nm.

The stoichiometry of the films (Fe/O ratio) was estimated by XPS from the ratio of the Fe $2p$ and O $1s$ core level areas af-

ter Shirley background subtraction and correction by the corresponding sensitivity factors[30]. The stoichiometric evaluation has only been done with XPS spectra where a metallic iron component (Fe^0) is not observed, because the strong asymmetry of the Fe^0 component and the intense overlap with the Fe^{2+} components preclude the rigorous estimation of the area of the latter.

1.2 Theoretical

We have performed first principles calculations based on the density functional theory including an effective on-site Coulomb repulsion term (U-J) following the Dudarev approach[32,33]. The conditions of the calculations have been chosen departing from the optimized values determined for bulk FeO[6]: we use the projector-augmented wave (PAW) method with an energy cutoff of 400 eV, and the Perdew-Burke-Ernzerhof parametrization of the generalized gradient approximation modified for solids (PBEsol) for the exchange-correlation functional, with U-J= 4 eV. In the calculations of thin films, a Monhorst-Pack sampling of the Brillouin Zone has been performed, of $9\times9\times1$ during relaxations and $13\times13\times1$ for the final structures.

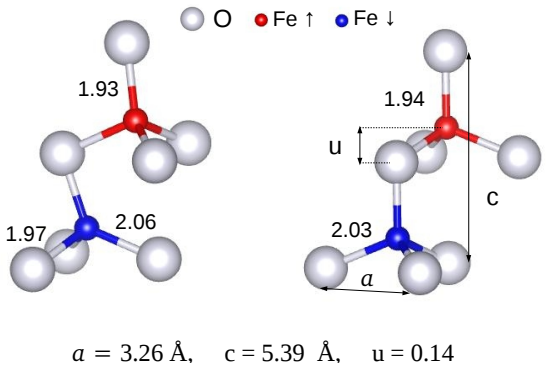

Fig. 1 Equilibrium WZ structure for the fully relaxed lattice (left) and the equivalent undistorted model (right). Both structures hold the same nominal lattice parameters (a, c, u), while differ in the lattice vectors and atomic positions. The different values of the interatomic Fe-O distances at each structure are provided in Å in the figure.

As it will be explained below in more detail, we have considered both tetrahedral and octahedral coordination sites at the FeO thin films. Only octahedral ones exist in the rocksalt (RS) lattice of stoichiometric bulk FeO. In order to have an adequate bulk reference also for the tetrahedral environment, we have modelled bulk FeO with the wurtzite and zinc-blende structures. After allowing full relaxation of the lattice vectors and interatomic positions, the differences between both kinds of structure regarding the interatomic distances, the electronic properties and the relative stability are minimal, thus we will restrict here to the WZ lattice. The electronic properties are similar to those of RS FeO: a wide gap insulator that orders antiferromagnetically with opposite spin orientations for Fe atoms at adjacent (0001) planes[34]. Also, in analogy to the magnetically driven distortion that exist in RS FeO, the equilibrium WZ structure is heavily distorted, as shown in figure 1. However, the most relevant features of both the RS and WZ bulk structures can still be retained in simplified undistorted models, that ease the simulation of thin films. We have adopted these undistorted lattices as our reference bulk structures, keeping the equilibrium lattice parameters, but using uniform interatomic spacings. In the case of the RS lattice this corresponds to a cubic symmetry with $a = 3.04$ Å and a unique Fe-O distance of 2.15 Å, while the WZ structure is detailed in figure 1. The resulting electronic properties are summarized in figure 2, obtained using Monhorst-Pack k-samplings of $7\times7\times7$ and $7\times7\times3$ for the RS and WZ bulk symmetries, respectively. The RS structure is more stable than the WZ one by 104.5 meV/atom, while for the distorted structures the difference is 82.9 meV/atom.

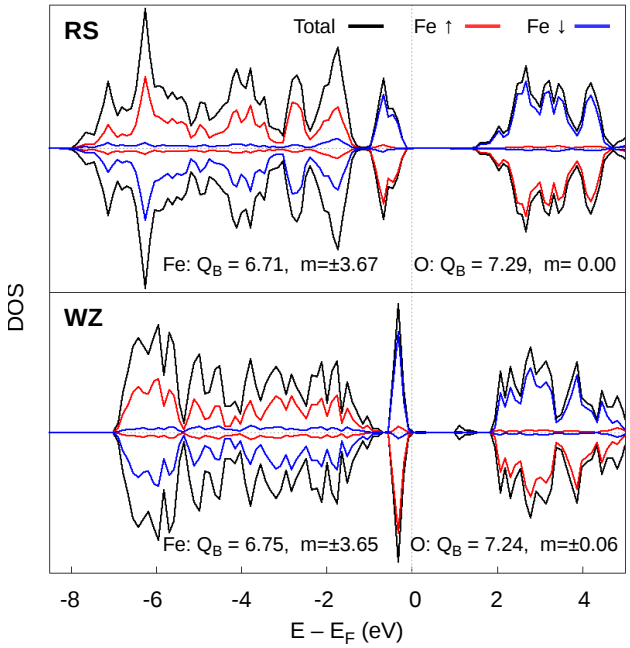

Fig. 2 Spin-polarized DOS (positive and negative values correspond to opposite spin orientations), and atomically resolved Bader charges (Q_B) and magnetic moments (m, in μ_B) in the undistorted RS (top) and WZ (bottom) bulk lattices.

The thin FeO(111) films have been modelled by slabs of different thicknesses that contain from 4 to 9 Fe planes, supported on a Ru(0001) layer that avoids the formation of an artificial dipole, and including a vacuum region of at least 17 Å. The inner planes are kept at the undistorted bulk-like positions, while we have allowed relaxation of the five outermost surface layers until the forces on all atoms were below 0.01 eV/Å. In all cases, bulk-like properties are recovered at the inner layers. We have considered both Fe- and O-terminated slabs, and explored alterations of the stacking sequence as will be explained in the next sections. Also the atomic positions at the Ru/FeO interface were optimized for an initial run at maximum slab thickness, and kept fixed for the rest of calculations. However, we have checked that in our computational model the interface structure does not introduce any effect on the conclusions about the surface properties presented here.

2 Experimental results

Although α-Fe_2O_3 corresponds to the most thermodynamically stable iron oxide phase, volatile elements like oxygen are frequently lost during the ablation process[35,36]. In our particular case, PLD in UHV environment does not allow to grow neither hematite thin films nor magnetite ones, unless 10^{-6} Torr oxygen is dosed during growth. Since our goal was to fabricate FeO films, no oxygen was dosed into the preparation chamber during deposition.

The substrate-target distance (d_{ts}), the deposition time and the temperature of the substrate were varied systematically in order to study the dependence of the film properties on these parameters. The pressure of the preparation chamber increased to 10^{-7} Torr during film growth. After preparation, the sample was transferred to the characterization chamber in UHV conditions, where LEED patterns, XPS and ISS spectra were acquired at room temperature.

In nanosecond PLD the morphology and composition of the films is strongly dependent on the laser wavelength, due to the prevalence of specific laser-target interaction and to the characteristics of the subsequent plume expansion[27,37]. Particularly for hematite, due to the low value of the linear absorption coefficient at 1064 nm, of around $\approx 1{\cdot}10^3$ cm^{-1} [27], the heated subsurface layer thickness is of the order of 10 μm. This target heated layer is much thicker than that of the layer that would be affected by laser irradiation with visible or UV wavelengths and is expected to affect the characteristics of the plume and the properties of the deposited films. The benefits of using an excitation wavelength of 1064 nm to grow Fe_3O_4 thin films from a hematite target have already been reported[27,28] justifying its use in our particular case.

We will first describe the features of a film grown under optimized conditions, and then the effect of the film thickness on their properties.

2.1 Optimum FeO growth parameters

Figure 3a shows the XPS spectrum of a 4.7 nm thick FeO film grown on Ru(0001) at 873 K, with a deposition time of 5 min and a distance (d_{ts}) of 4 cm from the target. The XPS spectrum was fitted considering a photoemission spin-orbit doublet at 709.7 (Fe $2p_{\frac{3}{2}}$) and 722.7 eV (Fe $2p_{\frac{1}{2}}$) with a FWHM of 3.7 eV. We added two additional components at binding energies of 712.7 eV and 725.4 eV to account for the broadening due to multiplet splitting, which is known to occur in the XPS spectrum of FeO[38,39]. The XPS spectrum also presents prominent shake-up satellite structure, which was fitted with two peaks at 716.4 eV and 729.8 eV. The presence of these satellite peaks and the binding energy difference of nearly 6 eV with respect to the main photoemission lines are clear evidence of Fe^{2+} [40].

The XPS spectrum was also used to determine the stoichiometry of the film. Surprisingly, and in spite of the large thickness well beyond the bilayer limit, the composition of the film was estimated to be Fe_xO ($x = 0.99 \pm 0.03$) which corresponds to an iron deficiency of ~1%. This means that the stoichiometry of the film is closer to the ideal value than most bulk samples, which present iron deficiencies of 5-15%.

Low energy electron diffraction (LEED) patterns were acquired to provide information about the surface structure of the film. A typical LEED pattern, shown in Figure 3b, reveals a 1×1 hexagonal pattern with six-fold symmetry. FeO, which has a cubic unit cell, should display three-fold symmetry along the (111) direction. Although each individual substrate terrace has three-fold symmetry[41], the average pattern from a macroscopic hcp Ru(0001) sample displays six-fold symmetry due to the averaging of different substrate terminations[42]. The pattern six-fold symmetry implies that the film is composed of twins. Whether the twins arise from growth on different substrate terraces or from growth on each terrace cannot be determined with our averaged LEED diffractometer.

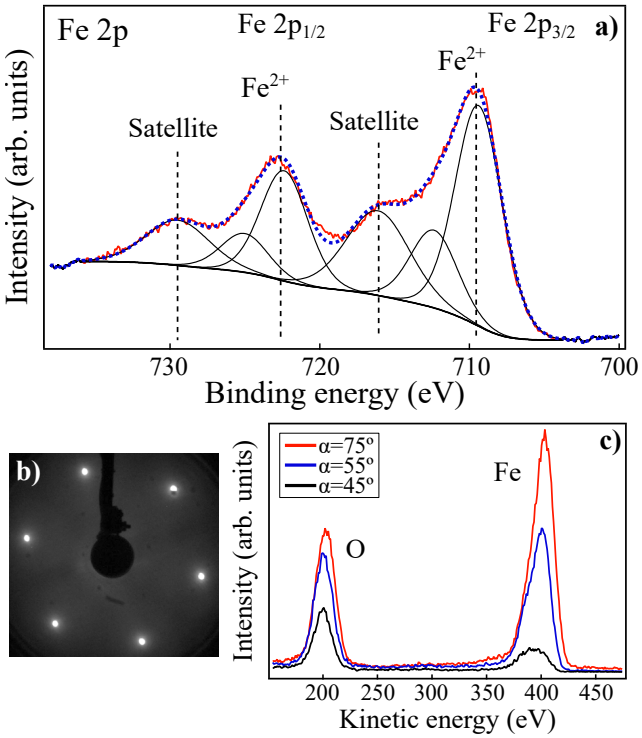

Fig. 3 a) XPS Fe 2p core level spectrum and b) LEED of a 4.7 nm thick FeO film grown on Ru(0001) by IR-PLD at 873 K for 5 min at a d_{ts} of 4 cm. c) ISS spectra acquired at three different beam angles of incidence: 75°, 55° and 45° of a FeO film deposited at 873 K, d_{ts} of 4 cm and z estimated in 14 nm. A lower angular value is related to higher grazing incidence of He^+ and higher surface sensitivity. The peak at 201.6 eV corresponds to oxygen and the peak at 403.6 eV to iron. The relative intensity of O to Fe increases at lower scattering angles, indicating an O-terminated surface.

It is worth noting that the FeO(111) surface presents no reconstruction. Comparing the spacing of the first-order diffracted spots with those of the Ru substrate, they are found to correspond to a distance of 0.307 nm, slightly larger than the in-plane lattice spacing of perfectly-stoichiometric bulk FeO[3]. The existence of Fe defects tends to contract the lattice, but the contraction is in the range of 0.01 nm for concentrations of vacancies around 15%.

To determine the surface termination of the grown films, ISS measurements were performed. Figure 3c shows the ISS spectra of a film deposited at 873 K, d_{ts} of 4 cm and z estimated in 14 nm

(extrapolated from the deposition time) at different beam angles of incidence. Two peaks are observed at 201.6 and 403.6 eV, where the former corresponds to O and the latter to Fe. Reducing the incidence angle, i.e. approaching more grazing incidence of the He^+ ions, the Fe contribution almost disappears whereas that of the O remains. This result strongly suggests that the FeO films are oxygen terminated.

Ex-situ AFM measurements were performed in order to obtain surface morphological information. The AFM images (included in the Supplementary Information) displayed a quite homogeneous film surface with a mean roughness of 0.6 ± 0.3 nm. LEED and XPS were performed after sample reintroduction into the UHV chamber to detect possible surface modifications. No LEED pattern was observed, and the Fe $2p_{\frac{3}{2}}$ and $2p_{\frac{1}{2}}$ photoemission peaks in the XPS spectrum shifted to higher binding energies, 710.7 and 723.8 eV, respectively. This shift, together with the appearance of a new satellite at 719.7 eV indicates the presence of Fe^{3+}. Thus, exposure to air of our films evidences the requirement of an UHV environment in order to obtain reliable data on unaltered surfaces of FeO films.

Thicker films keep a 1×1 LEED pattern and a characteristic Fe^{2+} XPS spectra. But while an almost stoichiometric composition of $Fe_{0.99}O$ was found on 4.7 nm thick films (see Figure 3), thicker films present a slightly decreasing Fe/O ratio. The 14 nm thick film had a composition of $Fe_{0.95}O$, with a lattice parameter of 0.300 nm. Thicker films, thus, are closer to bulk FeO as they are richer in iron defects (5% vs 1% on 4.7 nm thick film) and possess a smaller lattice parameter. However, the variations of the lattice parameter are much higher than those induced by Fe vacancies in bulk FeO.

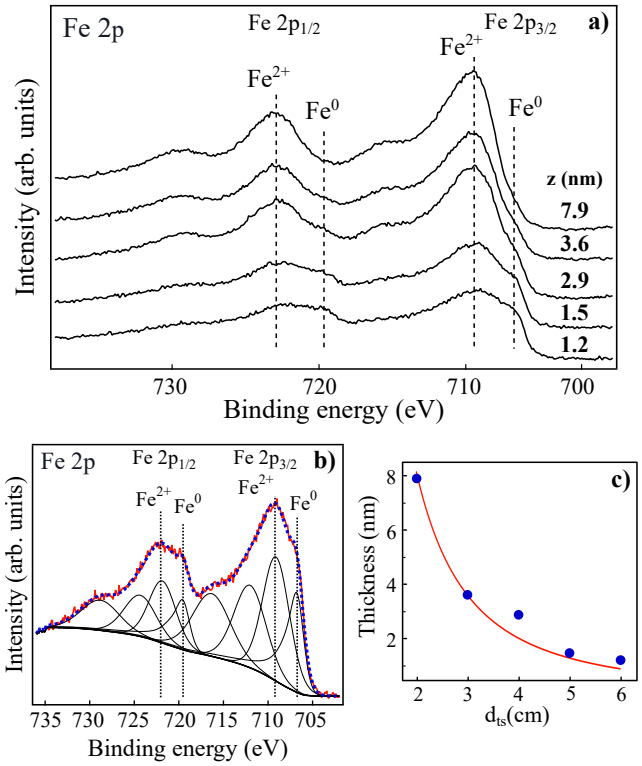

Fig. 4 a) XPS Fe $2p$ core level spectra of different iron oxide films grown by IR-PLD at 873 K, with a deposition time of 6 min and film thicknesses of: 7.9, 3.6, 2.9, 1.5 and 1.2 nm (from top to bottom). The corresponding d_{ts} are: 2,3,4,5 and 6 cm, respectively. b) Fit of the Fe $2p$ core level spectrum of the 1.2 nm thick film ($d_{ts} = 6$ cm) displaying FeO and metallic Fe contributions. c) Variation of the thickness of the FeO films with d_{ts}. The experimental results are shown by circles while the fit to an inverse-square law is shown by a continuous line.

2.2 Influence of film thickness

Figure 4a shows the XPS of the Fe $2p$ core level XPS spectra recorded from films deposited at different target-substrate distances, while maintaining the rest of the growth parameters fixed. The films grown at the shortest distance, 2 cm, present the typical Fe $2p$ spectra of FeO as shown in Figure 3. At larger d_{ts} values a second spin-orbit doublet appears at lower binding energies, 706.7 eV (Fe $2p_{\frac{3}{2}}$) and 719.7 eV (Fe $2p_{\frac{1}{2}}$), respectively, which is consistent with the presence of metallic iron. Figure 4b shows the fitting of the XPS spectrum of a 1.2 nm thick film to a combination of FeO and metallic Fe. This analysis gives a ratio of 86% FeO to 14% Fe. As can be observed on Figure 4c the film thickness is strongly reduced if the substrate-target distance is increased at a fixed deposition time. The evolution of the thickness with d_{ts} is well described by an inverse-square law characteristic of a free plume expansion [43].

Figures 5a-e show the corresponding LEED patterns of the FeO films whose XPS spectra are displayed on Figure 4a from top to bottom. The LEED pattern (Figure 5a) of the thickest film (7.9 nm) displays a 1×1 hexagonal pattern with six-fold symmetry like the pattern shown in Figure 3b. By decreasing the film thickness, additional spots start to appear around the first order spots (Figures 5b-e). These LEED patterns are similar to those obtained in ultrathin films grown by reactive-MBE [24] or sequential deposition and oxidation of iron [11], which have also been observed in real-space by scanning tunneling microscopy. In addition, these films present larger lattice parameters when the thickness is progressively diminished: from 0.307 nm for 4.7 nm thick films to 0.320 nm for subnanometric thicknesses. In fact, one and two atomic layers thick FeO films on Ru(0001) have a lattice spacing of 0.320 nm [11,24]. We interpret our results as the same moiré pattern arising from the coincidence of six FeO units on seven Ru atoms. Thus, the LEED patterns show an evolution from those of FeO for the thickest film (shortest d_{ts}) to Fe/Ru (or Ru) for the thinnest one (largest d_{ts}), while the moiré pattern of FeO/Ru is observed at intermediate thicknesses. The LEED results are thus fully consistent with the evolution of FeO to mixed FeO/Fe detected by XPS.

To confirm that the physical origin of the evolving composition is the thickness of the films (and not d_{ts}), deposits have been grown at a fixed d_{ts} and different deposition times. The corresponding XPS spectra are shown in Figure 6, where two different d_{ts} values have been explored, changing the deposition times to obtain films with the same thickness. As is clear from inspection of the spectra, the metallic iron component is related to the film thickness and not to d_{ts}. These results indicate that the Ru substrate at the given temperature induces the growth of metallic iron at the early stages of deposition. In a later stage, the growth

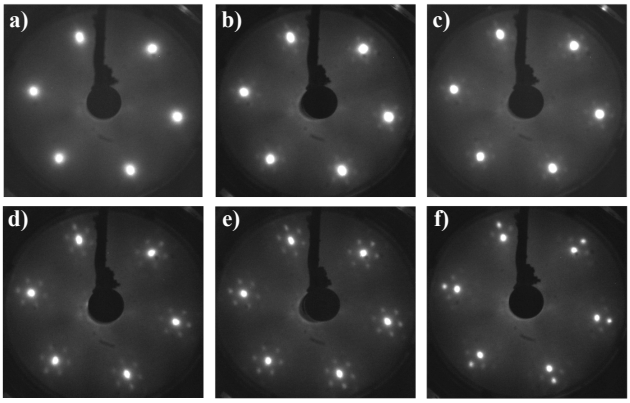

Fig. 5 LEED patterns from films grown at 873 K, with a deposition time of 6 min and thicknesses of: 7.9, 3.6, 2.9, 1.5 and 1.2 nm from a) to e). The last pattern labelled as f) corresponds to a 0.3 nm thick film prepared at 873 K, with a deposition time of 1 min and d_{ts} = 5 cm.

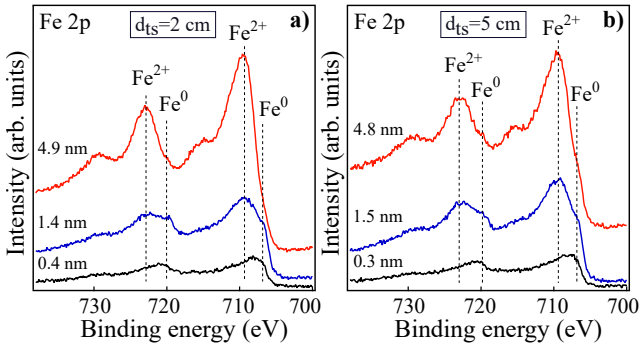

Fig. 6 XPS Fe 2p core level spectra of different iron oxide films grown by IR-PLD at 873 K. a) $d_{ts} = 2$ cm. The deposition times from top to bottom are: 3 min, 1 min and 10 s. The corresponding film thicknesses are: 4.9, 1.4 and 0.4 nm, respectively. b) $d_{ts} = 5$ cm. The deposition times from top to bottom are: 30, 6 and 1 min. The related film thicknesses are: 4.8, 1.5 and 0.3 nm, respectively.

of FeO takes place upon continuing deposition. It also suggests that even thick films with a FeO surface composition likely contain some metallic Fe at the film/substrate interface. The previous experiments have been performed on a Ru substrate heated at 873 K. A relatively high substrate temperature can produce the evaporation of oxygen from the surface in PLD[44]. Given that Ru is considered an essentially inert substrate in high vacuum conditions and Fe wetting on Ru is favoured by substrate heating, we speculate that oxygen evaporation takes place with higher probability at the interface with the Ru substrate than later on, when the FeO film is growing.

2.3 Effect of substrate temperature

Figure 7 shows the Fe 2p XPS core level spectra recorded from films grown at three different substrate temperatures. The XPS spectrum of the films prepared at 300 K stands out of the rest. Comparing it to the spectrum of FeO depicted in Figure 3, the main photoemission lines appear at slightly higher binding energies and the intensity of the characteristic Fe^{2+} shake-up satellites is also smaller. Together with an Fe/O ratio of 48/52 (i.e.

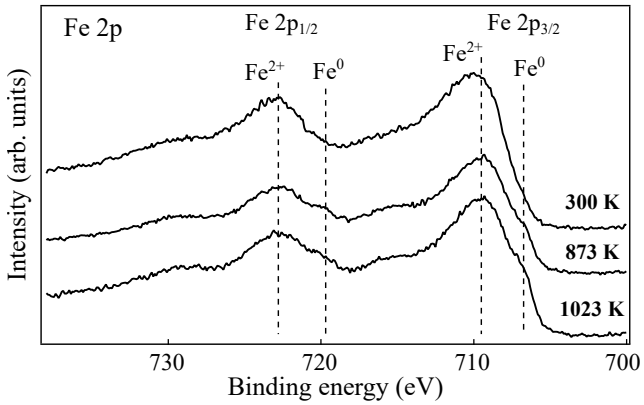

Fig. 7 XPS Fe 2p core level spectra of different iron oxide films grown at the substrate temperatures of 300 K, 873 K and 1023 K. The corresponding film thicknesses are 3.1, 2.7 and 2.1 nm, respectively. In all cases, d_{ts} was fixed at 4 cm and the deposition lasted for 3 min.

a higher oxygen content), the results suggest that the deposited film can contain some Fe^{3+}. The as-grown film does not show a LEED pattern, evidencing a disordered surface. After subsequent annealing to 873 K in vacuum the surface reflects a 2×2 LEED pattern with a reduced oxygen-oxygen lattice parameter of 0.302 nm, both suggesting a magnetite termination.

The films grown at 873 K and 1023 K both present XPS spectra characteristic of FeO plus an additional contribution at lower binding energies due to metallic iron, which increases from 3% at 873 K to 6% at 1023 K. They are both crystalline with a LEED displaying an hexagonal 1×1 pattern. In addition, these films are thinner than the one prepared at 300 K. This could be attributed in part to the formation of a more compact and ordered film as the temperature is increased.

Thus, by varying the temperature of the substrate, the surface composition of the sample (from a mixed Fe^{2+}/Fe^{3+} to only Fe^{2+}), the crystallinity (from a disordered surface to a monocrystalline one) and the surface structure of the films (from 2×2 to 1×1 surface termination) can be controlled.

We can conclude that the properties of films grown by PLD are highly dependent on the substrate temperature which governs the aggregation of ejected plume species on the heated surface. Previous studies in hematite and other materials[27,37] have shown that nucleation of crystalline material is favored by the use of IR laser wavelengths, that are poorly absorbed by the target, and by high substrate temperatures. For the results presented here, the combination of an IR wavelength and a heated Ru substrate seems to play a crucial role in the final characteristics of the FeO deposits obtained from an hematite target.

3 Theoretical results

The above results evidence the ability to grow stoichiometric FeO films well beyond the monolayer limit. These films show some intriguing features. One is the large expansion of the lattice parameter, that cannot be explained by merely attending to the absence of Fe vacancies. Other is the lack of any reconstruction, in spite of the polar nature of the surface. To shed some light in the origin of these results, we have performed *ab initio* calculations

of FeO(111) films, focusing on their surface properties. Following the information from LEED, we have modelled films with a (1×1) surface unit cell, considering both Fe- and O-terminations. However, the (1×1) symmetry admits the existence of stacking faults, similar to those observed at the O-ended CoO(111) surface apparently in connection to polarity compensation effects[29]. Then, in our simulations we have also allowed for the existence of a WZ-like coordination involving the three outermost planes, as shown in the right panel of figure 8 for an O-ended surface. First, we have compared the relative energies of Fe- and O-terminations under all possible surface stackings. As detailed in the Appendix, our results indicate that exposing an O layer is the favored situation, in excellent agreement with the results inferred from ISS measurements, and also with previous calculations[45]. In the following we will thus restrict to O-terminations.

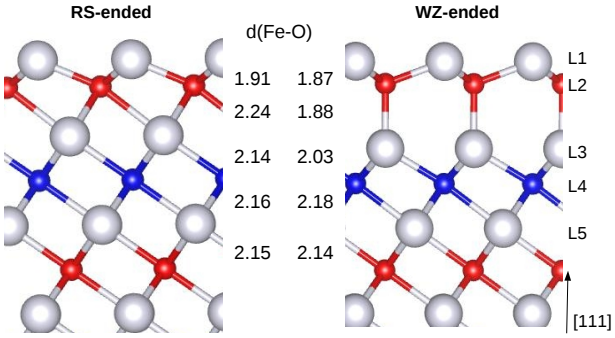

Fig. 8 Atomic structure of the O-ended FeO(111) surfaces under RS- and WZ-terminations. The interatomic Fe-O distances at the outermost planes of the 9-Fe layers thick slabs shown in figure 9 are provided in Å.

Figure 9 shows the electronic structure and atomically resolved Bader charges (Q_B) and magnetic moments at the surface layers of slabs containing 9 Fe planes. Below the fourth layer, bulk-like properties are essentially recovered, putting a limit in the extension of the surface region in the films. The surface features are common to all slab thicknesses considered. The left panel of the figure corresponds to the uniform RS stacking. The loss of neighbors of the surface O atoms increases the demand of charge to the remaining Fe neighbors, which empty all minority spin d states and lower the Q_B to 6.31. These are the electronic signatures of Fe^{3+} sites both in $Fe_{1-x}O$ and Fe_3O_4[6,46]. Thus the presence of these Fe atoms should manifest in additional peaks in the XPS spectra, contrarily to the experimental evidence. If we now regard the WZ-like termination shown in the right panel, the tetrahedral environment of the Fe subsurface atoms improves the charge compensation to the surface O atoms, introducing significant charge readjustments at the layers below. A slight iron metallic character is induced in the surface region, but both the occupancy of minority spin d states and the value of the Q_B over 6.5 are hints of Fe^{2+} sites[6,46]. Thus, the existence of a WZ-like termination can explain the experimental evidence of a (1×1) O-ended surface with only Fe^{2+}. This is an important result, that extends the existence of a stacking-fault reconstruction beyond the case of CoO(111).

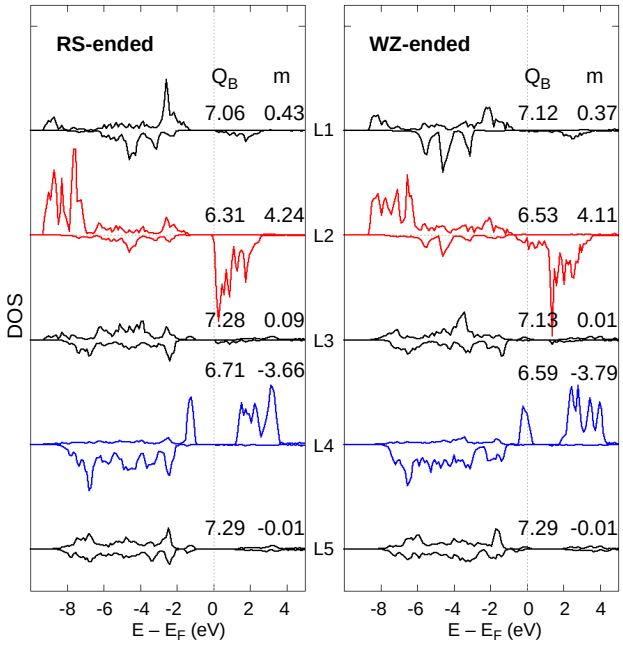

Fig. 9 Layer- and spin-resolved DOS of the RS- and WZ-terminations of the O-ended FeO(111) surfaces, also indicating the values of the Q_B and the magnetic moments (m, in μ_B), for the 5 outermost planes of a 9 Fe-layers thick slab. Layers are numbered from the surface (L1) to the bulk.

Another interesting feature of the WZ-ended surface, shared with the RS-termination and evidenced in figure 9, is the preservation of the layered antiferromagnetic order. Even at the monolayer limit, where the bulk magnetic order cannot be developed, FeO films show a clear prevalence of antiferromagnetic interactions[47]. Complex ferrimagnetism has been reported at reconstructed FeO(111) surfaces[21,48] or at intermediate film thicknesses beyond the bilayer and below 2 nm[12,22]. But in all cases, it was linked to a local environment different from stoichiometric FeO. Furthermore, in the thin films ferromagnetism seems to be a transient state in the evolution from the in-plane antiferromagnetism of the monolayer towards the bulk magnetic structure that already emerges at 2 nm thick films[23]. In our case, the charge readjustments and the magnetic uncompensation introduce an enhancement of the magnetic moments at the outermost layers, that might be observed by surface sensitive techniques. Non-collinear spin couplings or more complex magnetic orders could break the (1×1) periodicity.

The interatomic Fe-O distances shown in figure 8 evidence that there are also significant restructurations of the interlayer spacings. Obviously, the structural changes are deeper for the WZ-stacking, that tends to reduce considerably the bonds at the surface region. Comparing with the reference bulk values in figure 1, the contraction goes beyond the tetrahedral coordination environment, and is triggered by charge compensation effects. This is also present at the RS-ended surface, though the contractions are slighter, and rapidly compensated by expansions at the adjacent layers, introducing a decaying oscillatory variation of interlayer spacings. But in both structures, the bulk-like interatomic dis-

tances are essentially recovered below the fourth layer.

If we now compare the total energies of both surfaces, the WZ-stacking is favored over the uniform RS model by 30 meV in the 9 Fe layers thick slab. This energy difference is not negligible, but if we normalize to the number of atoms in both slabs it reduces to only 1 meV/atom, too low to explain the stability of the WZ-termination. However, different factors within our calculations may hinder the importance of the stabilization mechanism. First, both slabs only differ in the surface region, comprised by no more than 5 layers, so that the energy difference should be ascribed to only a few atoms in the structure. In addition, our slab construction forces us to use a common in-plane lattice parameter for all atomic planes, which in this case corresponds to the equilibrium RS bulk structure, $a(RS) = 3.04$ Å, lower than the experimental estimation for the thin films. Furthermore, a WZ symmetry would also favor a larger volume, as we have evidenced in figure 1. In order to address these issues, we have modelled again the O-ended slabs for all surface stackings and thicknesses using an expanded lattice parameter $a(WZ) = 3.26$ Å, that corresponds to our equilibrium value for the bulk structure of WZ FeO. As we keep the RS symmetry at the inner layers, the large volume expansion is not globally favored. Nevertheless, interesting information about the surface properties can be extracted. On one hand, and except for the slight narrowing of the DOS due to the expanded volume, the surface features described above remain essentially unaltered: the contraction of the outermost interatomic spacings, the emergence of Fe^{3+} (Fe^{2+}) features under RS (WZ) terminations, the continuity of the antiferromagnetic coupling with enhanced surface magnetic moments, and the recovery of the bulk-like properties below the fourth layer. Also, the universality of the surface properties for all thicknesses considered is preserved. On the other hand, interesting differences emerge from the relative stability of the WZ-termination over the RS-ended surface at fixed lattice parameter. This is shown in figure 10 as a function of the slab thickness. Two conclusions can be extracted: first, that an expanded lattice significantly favors the WZ termination. Second, that the energy differences, normalized to the number of atoms in the slabs, are higher the thinner the films, where the dominant energy terms come from the surface region.

As a further proof of the dominance of the surface terms in the energetics, we have also modelled slabs with an entire WZ structure, that is, keeping the WZ coordination throughout all layers. We have compared their energy to that of RS slabs with a WZ-ended surface. In this case the surfaces are similar, while the inner layers are in the respective WZ- and RS-equilibrium bulk forms. The corresponding energy difference for a thickness of 5 Fe layers favors the RS slab by 93 meV/atom, very close to the result found for the bulk structures. This demonstrates that a full WZ symmetry is not stable at reduced thicknesses. Thus, our theoretical results explain the origin of the unusual properties of the stoichiometric FeO(111) films, proving that they arise from the existence of a WZ-like environment at the surface. Preliminar calculations of $Fe_{1-x}O(111)$ surfaces indicate a tendency of Fe vacancies to occupy the outermost layers[34], favoring the usual evolution of FeO at increasing thickness to Fe_3O_4 or Fe_2O_3. This suggests that, besides our present growth conditions at an Fe-rich environment, the surface mechanism that stabilizes the WZ-termination also contributes to our ability to grow thick FeO films without Fe deficiency.

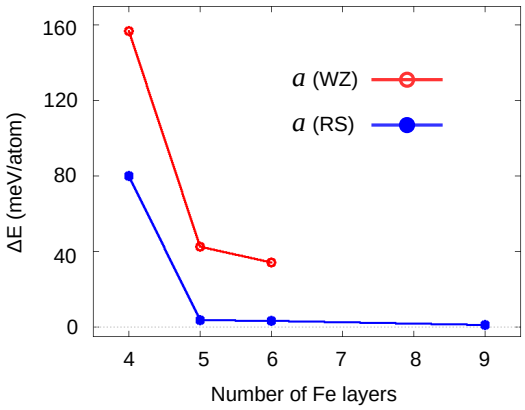

Fig. 10 Relative energy difference between the WZ- and RS-terminations, normalized to the number of FeO atoms in the slab, as a function of the slab thickness (measured by the number of Fe planes) for the two lattice parameters considered. Positive values correspond to stability of the WZ termination.

4 Conclusions

We have demonstrated the ability to grow single crystal FeO(111) ultrathin films on Ru(0001) with an improved stoichiometry over the bulk form, whose iron deficiency ranges 5-15% at room temperature. The choice of the growth technique, infrared pulsed laser deposition at a wavelength of 1064 nm, and the careful monitorization of the preparation conditions are crucial to achieve high crystallinity and controlled composition up to a record thickness of 8 nm. The films also present some unconventional features, namely, an expanded in-plane lattice parameter and (1×1) symmetry without Fe^{3+} at the topmost layers. Our first-principles calculations prove that these features arise from the existence of a WZ-like surface stacking, an unfrequent reconstruction. The WZ-surface environment is related to polarity compensations effects, but additionally it seems to play a primordial role in the stabilization of the stoichiometric FeO films beyond the bilayer limit.

These results extend the thickness range to stabilize stoichiometric FeO at ambient conditions, avoiding its transformation to the more thermodynamically stable Fe oxide forms, magnetite and hematite. Besides the intrinsic interest to design novel nanostructures beyond the known bulk phase diagram, these films will find application as building blocks in magnetoelectronic devices. In this sense, the preservation of the bulk-like antiferromagnetic order is a relevant issue. We have also shown that exposure to air causes surface damage that alters the film composition. However, there are previous evidences that a protective capping layer can be effective to preserve the stoichiometry when removing the film from UHV[17]. Further work is deserved to understand the effect of the capping on the local surface environment, and the consequences on the composition and electronic features.

Acknowledgments

This research was supported by the Spanish Ministry of Economy and Competitiveness (MINECO) through Projects MAT2012-38045-C04-01, MAT2012-38045-C04-04 and CTQ2013-43086-P, and Programa Geomateriales 2-CM (CAM, S2013/MIT-2914). M.O. thanks CSIC for contract, I.B. for the JAE program and L.M.-G. for an FPI contract with reference BES-2013-063396 from the MINECO. The VESTA package[49] has been used to create some of the original figures of this article.

Appendix: Relative stability of Fe- and O-terminations

To estimate the difference in surface energy between the Fe- and O-terminations, we have chosen slabs as those in figure11, formed by 9 FeO formula units plus an additional O layer in the O-ended case. Besides the WZ surface stacking shown in the figure, we have also considered slabs with uniform RS stacking.

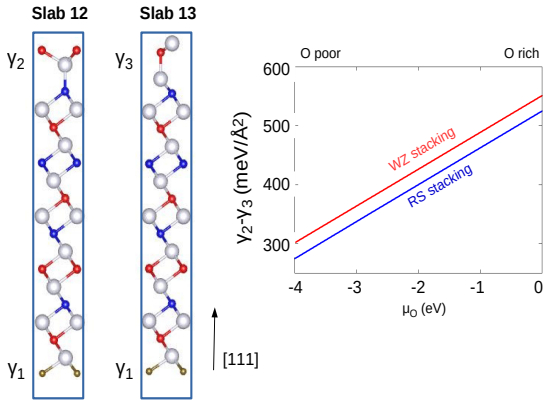

Fig. 11 (Left) Schematics of WZ-ended slabs used to compare the relative stability of Fe-ended (slab 12) and O-ended (slab 13) surfaces. The vertical size is shortened with respect to the actual vacuum region. (Right) Relative surface energy of the Fe-termination with respect to the O-ended one, for both WZ- and RS-surface stackings. The zero reference is set at the maximum value of the chemical potential.

Assuming standard approximations for *ab initio* thermodynamics[50], the surface energy of a slab with two dissimilar surfaces, i and j, can be expressed in terms of its total energy (E):

$$\gamma_i + \gamma_j = \frac{1}{A}[E - N_{Fe}\mu_{Fe} - N_O\mu_O] \quad (1)$$

with N the number of atoms of each chemical species and μ the respective chemical potentials. A takes into account the normalization per surface area. In case there is enough bulk material, the expression can be further simplified to depend only on the O chemical potential:

$$\gamma_i + \gamma_j = \frac{1}{A}[E - N_{Fe}E_{FeO} - \mu_O(N_O - N_{Fe})] \quad (2)$$

where E_{FeO} corresponds to the energy of bulk FeO per formula unit. The range of values of μ_O is bounded between an oxygen-rich limit defined by the total energy of a free oxygen molecule, where we set our energy zero, and an O-poor limit delimited by the heat of formation of bulk FeO. Thermochemical tables provide a value of -2.8 eV at ambient conditions[51], while our estimate from the Gibbs free energy of formation at T=0 K is -3.92 eV. Taking into account the uncertainty in the well-defined but approximate theoretical limits, we will plot the dependence of the surface free energies in the widest range of chemical potentials.

The slabs labelled 12 and 13 in the figure are identical except for the outermost surface layers, not only regarding their structure, but also the electronic and magnetic properties. Thus, we can assume that the bottom Ru terminations have identical surface energy, γ_1. To compare the contributions γ_2 and γ_3 we substitute values in equation 2 for both slabs, and then substract the resulting expressions. It is immediate that:

$$\gamma_2 - \gamma_3 = \frac{1}{A}[E_{12} - E_{13} + \mu_O] \quad (3)$$

where E_{12} and E_{13} are the total energies of the respective slabs. A positive value of this difference corresponds to a decreased stability of the Fe-ended surface over the O-ended one. Substituting the actual values from our calculations in equation 3, and taking into account the limits of μ_O, we arrive to the result shown in the graph of figure 11, that confirms the preference for O-ended surfaces under all stackings across the entire range of the chemical potential.

References

1 R. M. Cornell and U. Schwertmann, *The Iron Oxides*, John Wiley & Sons Ltd, Weinheim, 1997, p. 604.
2 S. Massidda, M. Posternak, A. Baldereschi and R. Resta, *Phys. Rev. Lett.*, 1999, **82**, 430.
3 R. Hazen and R. Jeanloz, *Rev. Geophys. Space Phys.*, 1984, **22**, 37.
4 F. Schrettle, C. Kant, P. Lunkenheimer, F. Mayr, J. Deisenhofer and A. Loidl, *Euro. Phys. J. B*, 2012, **85**, 164.
5 U. Wdowik, P. Piekarz, K. Parlinski, A. Oleś and J. Korecki, *Phys. Rev. B*, 2013, **87**, 121106(R).
6 I. Bernal-Villamil and S. Gallego, *Phys. Rev. B*, 2014, **90**, 192126.
7 V. Skumryev, S. Stoyanov, Y. Zhang, G. Hadjipanayis, D. Givord and J. Nogués, *Nature*, 2003, **423**, 850.
8 Y.-N. Sun, Z.-H. Qin, M. Lewandowski, E. Carrasco, M. Sterrer, S. Shaikhutdinov and H.-J. Freund, *J. Catal.*, 2009, **266**, 359.
9 Q. Fu, W. X. Li, Y. X. Yao, H. Y. Liu, H. Y. Su, D. Ma, X. K. Gu, L. M. Chen, Z. Wang, H. Zhang, B. Wang and X. H. Bao, *Science*, 2010, **328**, 1141–1144.
10 W. Weiss and W. Ranke, *Prog. Surf. Sci.*, 2002, **70**, 1–151.
11 G. Ketteler and W. Ranke, *J. Phys. Chem. B*, 2003, **107**, 4320–4333.
12 N. Spiridis, D. Wilgocka-Ślęzak, K. Freindl, B. Figarska, T. Giela, E. Młyńczak, B. Strzelczyk, M. Zając and J. Korecki, *Phys. Rev. B*, 2012, **85**, 075436.
13 F. Schedin, L. Hewitt, P. Morrall, V. N. Petrov, G. Thornton, S. Case, M. F. Thomas and V. M. Uzdin, *Phys. Rev. B*, 1998, **58**, R11861.
14 F. Bertram, C. Deiter, O. Hoefert, T. Schemme, F. Timmer, M. Suendorf, B. Zimmermann and J. Wollschläger, *J. Phys. D:*

Appl. Phys., 2012, **45**, 395302.
15 I. Ermanoski and G. Kellogg, *Surf. Sci.*, 2013, **614**, 1–11.
16 B. Santos, E. Loginova, A. Mascaraque, A. K. Schmid, K. F. McCarty and J. de la Figuera, *J. Phys. Cond. Matt.*, 2009, **21**, 314011.
17 S. Couet, K. Schlage, K. Saksl and R. RÃűhlsberger, *Phys. Rev. Lett.*, 2008, **101**, 056101.
18 J. Gurgul, E. Mlynczak, N. Spiridis and J. Korecki, *Surf. Sci.*, 2012, **606**, 711.
19 H. Galloway, J. Benítez and M. Salmeron, *J. Vac. Sci. Technol. A*, 1994, **12**, 2302.
20 D. Cappus, M. Hassel, E. Neuhaus, M. Heber, F. Rohr and H.-J. Freund, *Surf. Sci.*, 1995, **337**, 268.
21 K. Mori, M. Yamazaki, T. Hiraki, H. Matsuyama and K. Koike, *Phys. Rev. B*, 2005, **72**, 014418.
22 G. Beach, F. Parker, D. Smith, P. Crozier and A. Berkowitz, *Physical Review Letters*, 2003, **91**, 267201.
23 N. Spiridis, M. Zając, P. Piekarz, A. Chumakov, K. Freindl, J. Goniakowski, A. Kozioł-Rachwał, K. Parliński, M. Ślęzak, T. Ślęzak, U. Wdowik, D. Wilgocka-Ślęzak and J. Korecki, *Phys. Rev. Lett.*, 2015, **115**, 186102.
24 I. Palacio, M. Monti, J. F. Marco, K. F. McCarty and J. d. l. Figuera, *J. Phys.: Cond. Matt.*, 2013, **25**, 484001.
25 *Pulsed Laser Deposition of Thin Films: Applications-Led Growth of Functional Materials*, ed. R. Eason, John Wiley & Sons, Inc., 2007.
26 P. Willmott, *Prog. Surf. Sci.*, 2004, **76**, 163–217.
27 M. Sanz, M. Oujja, E. Rebollar, J. F. Marco, J. de la Figuera, M. Monti, A. Bollero, J. Camarero, F. J. Pedrosa, M. García-Hernández and M. Castillejo, *Appl. Surf. Sci.*, 2013, **282**, 642–651.
28 M. Monti, M. Sanz, M. Oujja, E. Rebollar, M. Castillejo, F. J. Pedrosa, A. Bollero, J. Camarero, J. L. F. Cuñado, N. M. Nemes, F. J. Mompean, M. Garcia-Hernández, S. Nie, K. F. McCarty, A. T. N'Diaye, G. Chen, A. K. Schmid, J. F. Marco and J. d. l. Figuera, *J. App. Phys.*, 2013, **114**, 223902.
29 W. Meyer, D. Hock, K. Biedermann, M. Gubo, S. Müller, L. Hammer and K. Heinz, *Phys. Rev. Lett*, 2008, **101**, 01603.
30 D. Briggs and M. P. Seah, *Practical Surface Analysis, Auger and X-ray Photoelectron Spectroscopy*, Wiley, 1990.
31 C. Powel and A. Jablonski, *NIST Electron Effective-Attenuation-Length Database Version 1.3*, National Institute of Standards and Technology, Gaithersburg, MD, 2011.
32 G. Kresse and J. Furthmüller, *Phys. Rev. B*, 1996, **54**, 11169.
33 S. Dudarev, G. Botton, S. Savrasov, C. Humphreys and A. Sutton, *Phys. Rev. B*, 1998, **57**, 1505.
34 I. B. Villamil, *PhD thesis*, Instituto de Ciencia de Materiales de Madrid/UAM, Madrid, 2015.
35 H. Christen and E. G., *J. Phys.: Condens. Matter*, 2008, **20**, 264005–264021.
36 D. Yokoyama, K. Namiki, H. Fukasawa, J. Miyazaki, K. Nomura and Y. Yamada, *J. Radioanal. Nucl. Chem.*, 2007, **272**, 631–638.
37 M. Sanz, M. Walczak, M. Oujja, A. Cuesta and M. Castillejo, *Thin Solid Films*, 2009, **517**, 6546–6552.
38 N. S. McIntyre and D. G. Zetaruk, *Anal. Chem.*, 1977, **49**, 1521–1529.
39 A. P. Grosvenor, B. A. Kobe, M. C. Biesinger and N. S. McIntyre, *Surf. Inter. Anal.*, 2004, **36**, 1564–1574.
40 T. Yamashita and P. Hayes, *Appl. Surf. Sci.*, 2008, **254**, 2441–2449.
41 J. de la Figuera, J. Puerta, J. Cerda, F. El Gabaly and K. McCarty, *Surf. Sci.*, 2006, **600**, L105–L109.
42 G. Held, S. Uremović and D. Menzel, *Surface Science*, 1995, **331–333, Part B**, 1122–1128.
43 S. Anisimov, D. Bäuerle and B. Lukyanchuk, *Phys. Rev. B*, 1993, **48**, 12076–12081.
44 R. Kumar, G. Kumar and A. Uhmar, *J. Nanosci. Nanotechnol.*, 2014, **14**, 1911–1930.
45 Y. Li, K. Yao, Z. Liu and G. Gao, *Phys. Rev. B*, 2005, **72**, 155446.
46 I. Bernal-Villamil and S. Gallego, *J. Phys.: Condens. Matter*, 2015, **27**, 012001.
47 L. Giordano, G. Pacchioni, J. Goniakowski, N. Nilius, E. D. L. Rienks and H. J. Freund, *Phys. Rev. B*, 2007, **76**, 075416.
48 H.-J. Kim, J.-H. Park and E. Vescovo, *Phys. Rev. B*, 2000, **61**, 15284.
49 K. Momma and F. Izumi, *J. Appl. Crystallogr.*, 2011, **44**, 1272–1276.
50 K. Reuter and M. Scheffler, *Phys. Rev. B*, 2001, **65**, 035406.
51 *CRC Handbook of Chemistry and Physics*, CRC Press, Boca Raton, FL, 1995.